Preprints.org

Article

Not peer-reviewed version

Multi-Step Simulations of Ionized Metal Physical Vapor Deposition to Enhance the Plasma Formation Uniformity

Cheongbin Cheon , Min Young Hur , Ho Jun Kim * , Hae June Lee *

Posted Date: 9 December 2024

doi: 10.20944/preprints202412.0631.v1

Keywords: ionized metal physical vapor deposition; multi-step simulation; sputter yield; target rotation

Preprints.org is a free multidisciplinary platform providing preprint service that is dedicated to making early versions of research outputs permanently available and citable. Preprints posted at Preprints.org appear in Web of Science, Crossref, Google Scholar, Scilit, Europe PMC.

Copyright: This open access article is published under a Creative Commons CC BY 4.0 license, which permit the free download, distribution, and reuse, provided that the author and preprint are cited in any reuse.

Preprints.org (www.preprints.org) | NOT PEER-REVIEWED | Posted: 9 December 2024 doi:10.20944/preprints202412.0631.v1

Disclaimer/Publisher's Note: The statements, opinions, and data contained in all publications are solely those of the individual author(s) and contributor(s) and not of MDPI and/or the editor(s). MDPI and/or the editor(s) disclaim responsibility for any injury to people or property resulting from any ideas, methods, instructions, or products referred to in the content.

Article

Multi-Step Simulations of Ionized Metal Physical Vapor Deposition to Enhance the Plasma Formation Uniformity

Cheongbin Cheon [1,2], Min Young Hur [3], Ho Jun Kim [4,*] and Hae June Lee [1,*]

[1] Department of Electrical Engineering, Pusan National University, Busan 46241, Republic of Korea; cjscjdqls@pusan.ac.kr
[2] Semiconductor Process and Equipment Contract Department, Pusan National University, Busan 46241, Republic of Korea
[3] Semiconductor Research and Development Center, Samsung Electronics Company, Ltd., Suwon 16677, Republic of Korea; minyoung.hur@samsung.com
[4] Department of Mechanical Engineering, Hanyang University ERICA Campus, Gyeonggi 15588, Republic of Korea
* Correspondence: haejune@pusan.ac.kr and hojunkim9158@hanyang.ac.kr

Abstract: The ionized metal physical vapor deposition (IMPVD), which is operated at a very low pressure to take advantage of the metal sputtering effect on the target surface, has unique properties compared with the conventional DC magnetron sputtering. In this study, we investigated the effect of the rotating magnetic field on the plasma formation of the IMPVD to enhance the deposition uniformity. A two-dimensional particle-in-cell Monte Carlo simulation utilizes the exact cross-section data of the Cu ion collisions and calculates the particle trajectories under specific magnetic field profiles. This new methodology gives guidance for the design of the magnetic field profiles of IMPVD and an understanding of the physical mechanism.

Keywords: ionized metal physical vapor deposition; multi-step simulation; sputter yield; target rotation

1. Introduction

Magnetron sputtering sources have been used in the semiconductor industry to form thin metal films during deposition [1,2]. Direct current (DC) magnetron sputtering is primarily used to deposit metal thin films [3]. When ions accelerated by the potential distribution collide with the target metal with sufficient energy, they dislodge metal atoms. These sputtered atoms then travel to the substrate and are deposited. RF magnetron sputtering is mainly used to deposit thin films of insulating materials because it resolves the issue of charge accumulation on the dielectric, which can complicate the process [4–6]. However, radiofrequency (RF) magnetron sputtering can also be used for metal deposition processes. It allows for easier discharge, extends the target's lifespan, and enables ionized sputtered metal to reach the substrate, forming the coating material. In these processes, both neutral particles and ions are deposited onto the substrate, enhancing uniformity and adhesion, respectively [7]. This characteristic of RF magnetron sputtering is distinct from that of general DC magnetron sputtering, and it is a feature of ionized metal physical vapor deposition (IMPVD). Previous studies have shown that the ionization rate of the sputtered metal in IMPVD can be up to 50% [8], and voids may form if the ionization fraction is too low during metal deposition [9]. Therefore, a gas discharge analysis is crucial to investigate the reactions contributing to the ionization of sputtered metal in the IMPVD process and to identify factors affecting deposition uniformity.

If the magnetron sputtering process continues, the metal target will eventually wear out and need to be replaced, which poses a problem in terms of cost and time. To address this, research has been conducted on rotating the magnet [10] or combining both rotation and revolution [11]. Additionally, the magnet can be configured in a cardioid shape and rotated to ensure that the target wears more evenly, thereby reducing the replacement cycle [12]. Since the magnetic confinement of electrons and the increased plasma density due to ionization in the region contribute to the erosion of targets, it is essential to conduct research using particle-in-cell (PIC) simulations that can effectively

© 2024 by the author(s). Distributed under a Creative Commons CC BY license.

Preprints.org (www.preprints.org) | NOT PEER-REVIEWED | Posted: 9 December 2024 doi:10.20944/preprints202412.0631.v1

explain the gyromotion and finite Larmor radius effects in magnetron sputtering devices, which are partially magnetized systems. In a previous study, the ion energy-angle distribution (IEAD) [13] and the IEAD analysis of negative ions [14], based on gas pressure changes in DC magnetron sputtering devices, were investigated. Additionally, studies were conducted to compare the IEAD and yield for eroded targets and flat targets [15], and to investigate the effects of heating profiles, electron drift motion [16], and rotating structures [17].

To accurately simulate the magnetron sputtering equipment, three stages of research are required: (i) analysis of the behavior and spatial distribution of plasmas, (ii) analysis of the interaction between ions generated in the plasma and the target surface, and (iii) analysis of the behavior and deposition of neutral/charged gas emitted from the plasmas. To this end, this study performs multi-step simulations with magnetic field calculation, PIC simulation, yield calculation in polar coordinates, direct simulation Monte Carlo (DSMC), and deposition distribution calculation. For the IMPVD process, the spatial distribution analysis of charged and neutral particles is performed by simulating the RF magnetron sputtering source with rotating magnets.

2. Simulation Procedures

Multi-step simulations to obtain the deposition profile for the IMPVD process with the RF magnetron sputter source involve several procedures, and the corresponding flowchart is shown in Fig. 1.

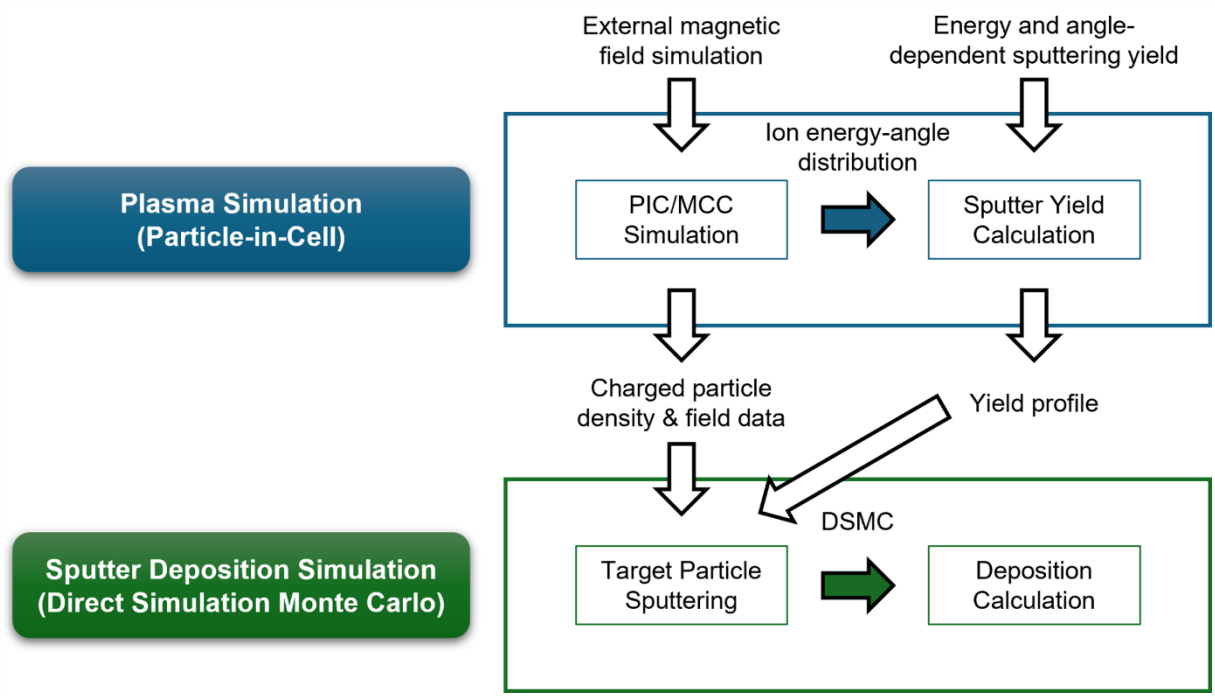

Figure 1. Flowchart of the multi-step simulation.

2.1. External Magnetic Field Simulation by Permanent Magnets and Electromagnetic (EM) Coil:

In order to perform a 2-dimensional (2D) plasma simulation using a 3D permanent magnet, the magnetic field is calculated at different angles, and independent plasma simulations are conducted for each angle. Plasma simulations using a rotating cardioid-shaped magnet can be analyzed by utilizing the symmetry of the results at 0°, 15°, 30°, 45°, 60°, 75°, and 90°. Finite Element Method Magnetics (FEMM) [18], a freeware, and Computer Simulation Technology (CST) Studio Suite [19], a commercial software, are used to calculate the magnetic field distribution of the permanent magnets and electromagnetic coils. The calculated magnetic field shape is stored at each grid location of the 2D PIC simulation, and the simulation is then carried out.

2.2. Inductively Coupled Plasma (ICP) Source Simulation:

Preprints.org (www.preprints.org) | NOT PEER-REVIEWED | Posted: 9 December 2024 doi:10.20944/preprints202412.0631.v1

For the PIC simulation, an in-house code used in several studies is employed [13–17,20–22]. Since an ICP antenna is present, plasma simulation is first performed for the ICP source to reduce simulation time. To calculate the EM field of the ICP module, the magnetic vector potential is computed from the combined equations of Ampere's circuital law and Faraday's law. Once the simulation converges, field and particle data are stored and used as the input for the next simulation.

2.3. RF Magnetron Sputtering Simulation:

The PIC simulations converge again by adding the external magnetic field, DC bias, and RF bias to the plasmas formed by the ICP source. The main routine of the PIC simulation includes external circuit calculation, field solver, field-to-particle weighting, particle mover, Monte Carlo collision (MCC), boundary, and particle-to-field weighting. Once the simulation converges, the IEAD and sputter yield at the target surface can be determined.

2.4. Yield Calculation:

Using the ion bombardment results and sputter yield results from the PIC simulations for different angles, ion bombardment and yield due to target rotation are calculated using polar coordinates. This results in the same profile for all angles.

2.5. Sputtered Target Particle Simulation:

The direction and speed of the sputtered metal are determined from the yield and ion bombardment. The target particles have the ejection angle η to the surface with the angular distribution of $\cos\eta$-shape [23], and their thermal speed follows a Maxwellian distribution based on the target's temperature. The target temperature is assumed to be 500 K. Sputtered particles travel toward the substrate and undergo collision processes, which are calculated using particle-particle and particle-background Monte Carlo collisions. The electric and magnetic fields also influence ionized sputtered particles. From this, the ions and neutral species that reach the wafer are counted in polar coordinates.

2.6. Deposition Profile Calculation

The DSMC results calculated for each angle with respect to the magnetic field are summed. Using the symmetry, the deposition profiles of the neutral atoms and ions are calculated.

3. DC Magnetron Sputtering System with a Simple Consideration of the Magnet Configuration

The simulation domain of the DC magnetron sputtering system and the magnetic field intensity distribution, which is obtained by simply shifting the position of the permanent magnet, are shown in Fig. 2. The magnetic field distribution due to the permanent magnets and EM coils was calculated using FEMM. The system size is $0.550\ \text{m} \times 0.512\ \text{m}$, the grid size is $0.001\ \text{m} \times 0.001\ \text{m}$, the time step is 1×10^{-11} s, the gas is argon at 0.3 mTorr, the DC power is 1 kW, and the secondary electron emission coefficient is 0.2.

As shown in Fig. 3, electrons are confined in regions with high magnetic field strength. Since these electrons generate ions through ionization in these regions, a plasma formation profile is observed in the areas with higher magnetic field strength. As can be seen from the potential and electron density distributions, the magnetic mirror effect caused by the magnet location at a lower position on the y-axis causes electrons to move toward the ground region at $y = 0$, resulting in a broader electron distribution profile compared to the electron distribution that is confined by the magnets located at higher positions on the y-axis. Furthermore, the magnetic field formed by the EM coils causes the narrower electron distribution at the higher position on the y-axis. Although the field strength is about 1/10 of that formed by the permanent magnet, it can create an X-point where the field strength becomes zero, which causes the electrons to move toward the EM coils. Magnetic mirror effect is also observed in this region. Therefore, in Case 1-3, the voltage drop is relatively smaller near the magnet located at a lower position on the y-axis, while in Case 4, the voltage drop is relatively smaller near the magnet located at a higher position on the y-axis. In other words, in Case 1-3,

Preprints.org (www.preprints.org) | NOT PEER-REVIEWED | Posted: 9 December 2024 doi:10.20944/preprints202412.0631.v1

electron loss occurs toward the $y = 0$ boundary. In Case 4, however, electron movement due to the closer X-point causes the potential distribution near the permanent magnet to change. The distribution of the strong voltage drop near the target affects the energy and angle of the ions striking the target, and this can be used to calculate the sputtered target particle yield.

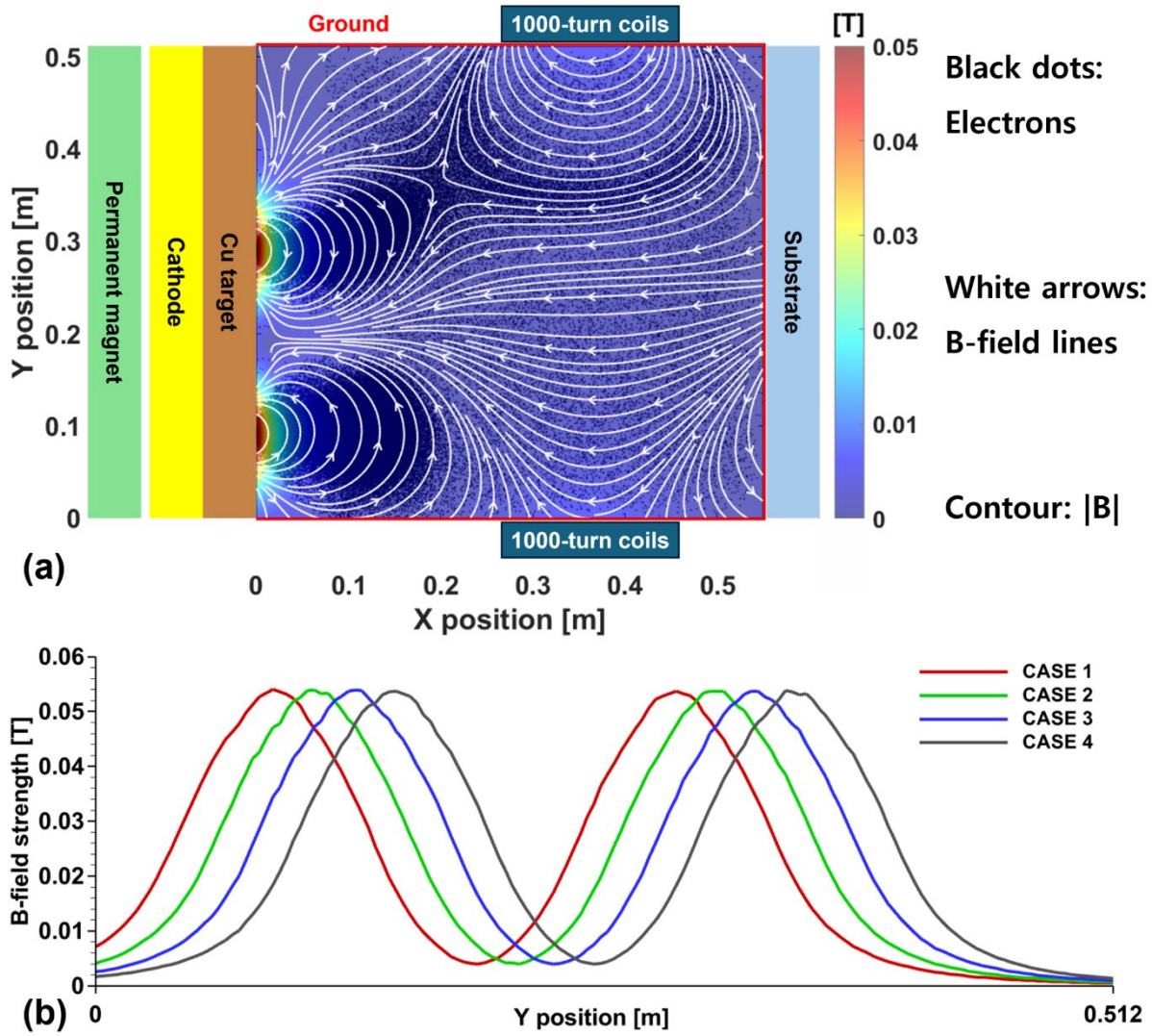

Figure 2. (a) Schematic DC magnetron sputtering device diagram. The magnetic field strength, flux lines, and electron spatial distribution are shown following the arrangement of permanent magnets and EM coils. (b) Magnetic field strength at the target surface when the position of the magnets is shifted.

Preprints.org (www.preprints.org) | NOT PEER-REVIEWED | Posted: 9 December 2024 doi:10.20944/preprints202412.0631.v1

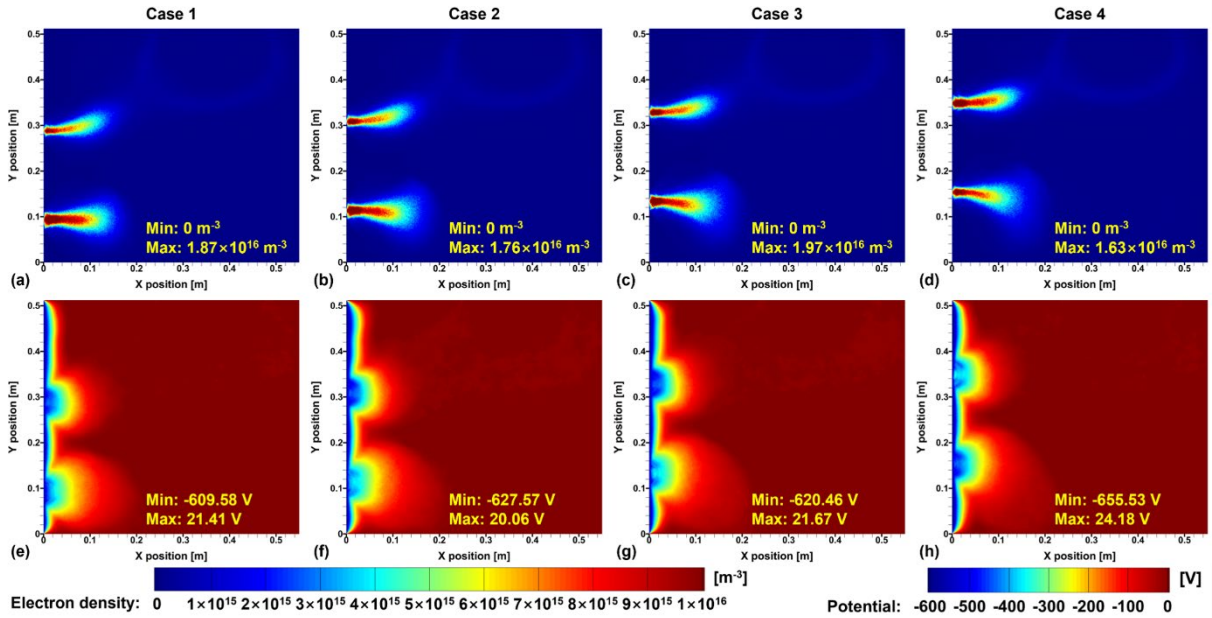

Figure 3. (a-d) Electron density distributions and (e-h) potential distributions for each case.

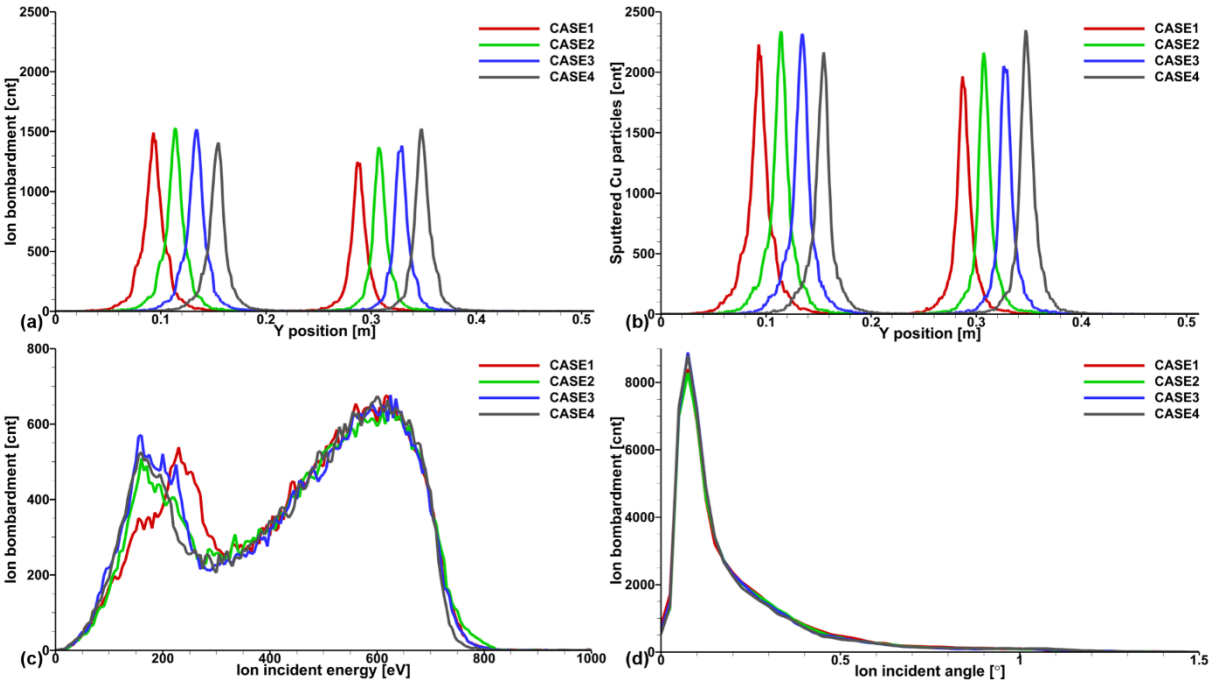

Figure 4. (a) Ion bombardment incident on the target, (b) amount of sputtered material from the target, (c) amount as a function of ion incident energy, and (d) amount of ion bombardment as a function of incident angle.

Figure 4 shows the ion bombardment incident on the Cu target, the amount of sputtered metal resulting from it, and the energy and angle distributions of the incident ions. The spatial distribution of ions incident on the target is high in the region where the magnets are located due to the higher plasma density, and the magnetic field distribution controls it. The energy of ions striking the target is determined by the potential difference from the ionization region to the target surface, but the incident ion angle does not vary significantly according to the magnetic field distribution. The effect of the voltage drop is much more significant, so most ions have an angle of less than 1°. Furthermore, due to the collision of high-energy Ar ions, more than one target particle is sputtered by a single ion.

4. RF Magnetron Sputtering System with the Rotating Magnets

Preprints.org (www.preprints.org) | NOT PEER-REVIEWED | Posted: 9 December 2024 doi:10.20944/preprints202412.0631.v1

As shown in the simple DC magnetron sputtering results, the incident ion energy contributing to the generation of sputtered metal is affected by the magnetic field distribution and plasma distribution. Yamamura proposed that the yield depends on normal incident ion energy [24]. Using this, Eckstein proposed a yield incorporating angular dependence [25,26]. To calculate the sputter yield dependent on this IEAD, the Yamamura and Eckstein formulae were incorporated into the PIC code. Additionally, the data for calculating the sputtering and reaction of the Cu target in argon plasma using sputter yield through DSMC is presented in Table 1.

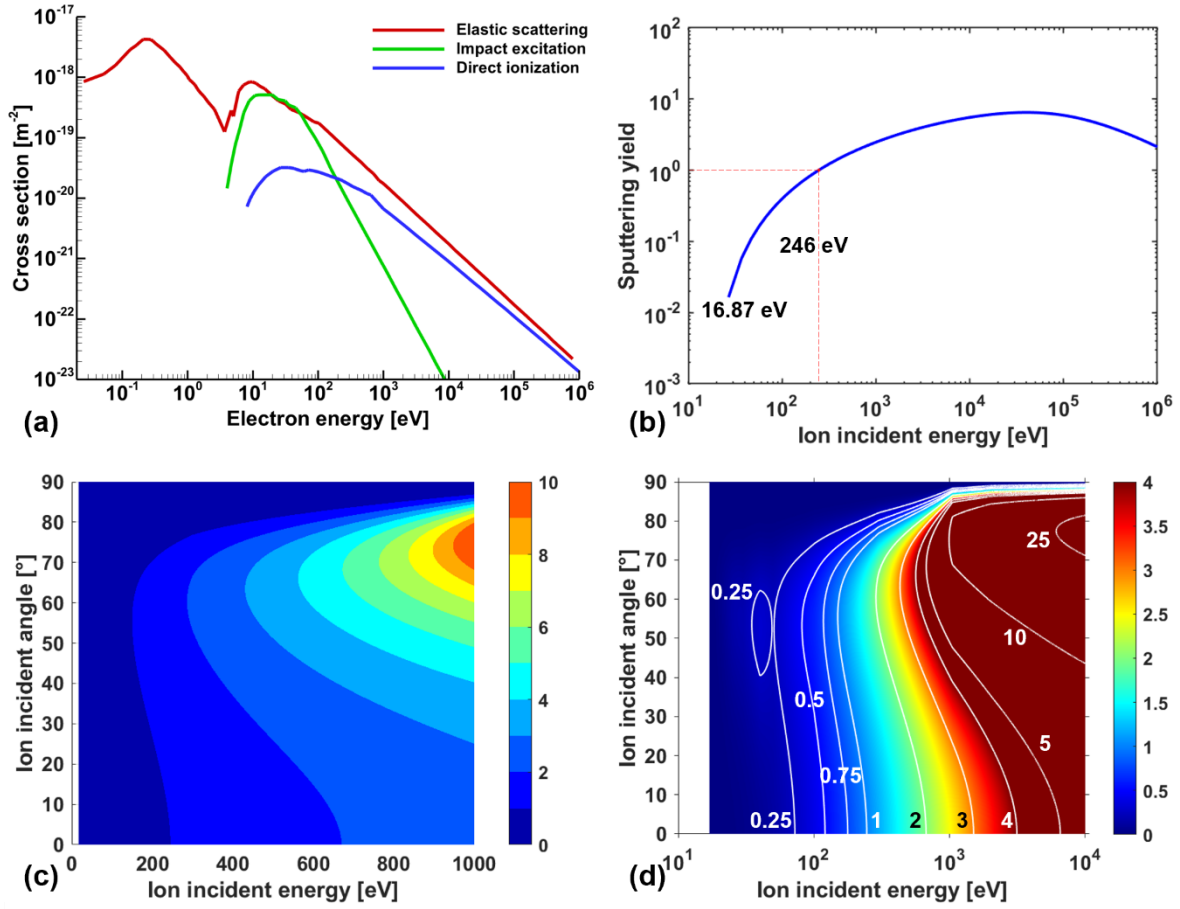

Figure 5. (a) Collision cross sections of Cu atoms dependent on electron energy, (b) Yamamura formula, and (c-d) Eckstein formula.

The cross-sections for the reaction between electrons and copper atoms are shown in Fig. 5a. Additionally, Fig. 5b shows the Yamamura formula, where sputtering occurs only when the ion incident energy exceeds the threshold energy of approximately 16.87 eV. When the normal incident ion energy reaches about 246 eV, the sputtering yield becomes 1. Fig. 5d represents the Eckstein formula considering angular dependency, while Fig. 5c shows the Eckstein formula for the region of interest.

Preprints.org (www.preprints.org) | NOT PEER-REVIEWED | Posted: 9 December 2024 doi:10.20944/preprints202412.0631.v1

Table 1. Reaction sets for the Ar plasmas with the Cu target.

Reaction Equation	Name	Data (k or σ)	Ref.
$e + Cu \rightarrow e + Cu$	Elastic scattering	σ [1]	[27]
$e + Cu \rightarrow e + Cu^*$	Electron impact excitation	σ [1]	[27]
$e + Cu \rightarrow e + e + Cu^+$	Direct ionization	σ [1]	[27]
$Ar + Cu \rightarrow Ar + Cu$	Elastic collision	$\sigma = 1.1664 \times 10^{-20}$ m^2	a [2]
$Ar^+ + Cu \rightarrow Ar + Cu^+$	Charge exchange	$k = 1.0 \times 10^{-15}$ m^3/s	a [2]
$Cu^+ + Cu \rightarrow Cu + Cu^+$	Charge exchange	$k = 6.0 \times 10^{-16}$ m^3/s	[28]
$Cu^+ + Ar \rightarrow Cu^+ + Ar$	Elastic collision	$\sigma = 1.1664 \times 10^{-20}$ m^2	a [2]

[1] Cross section data corresponding to Fig. 5a. [2] Estimated values.

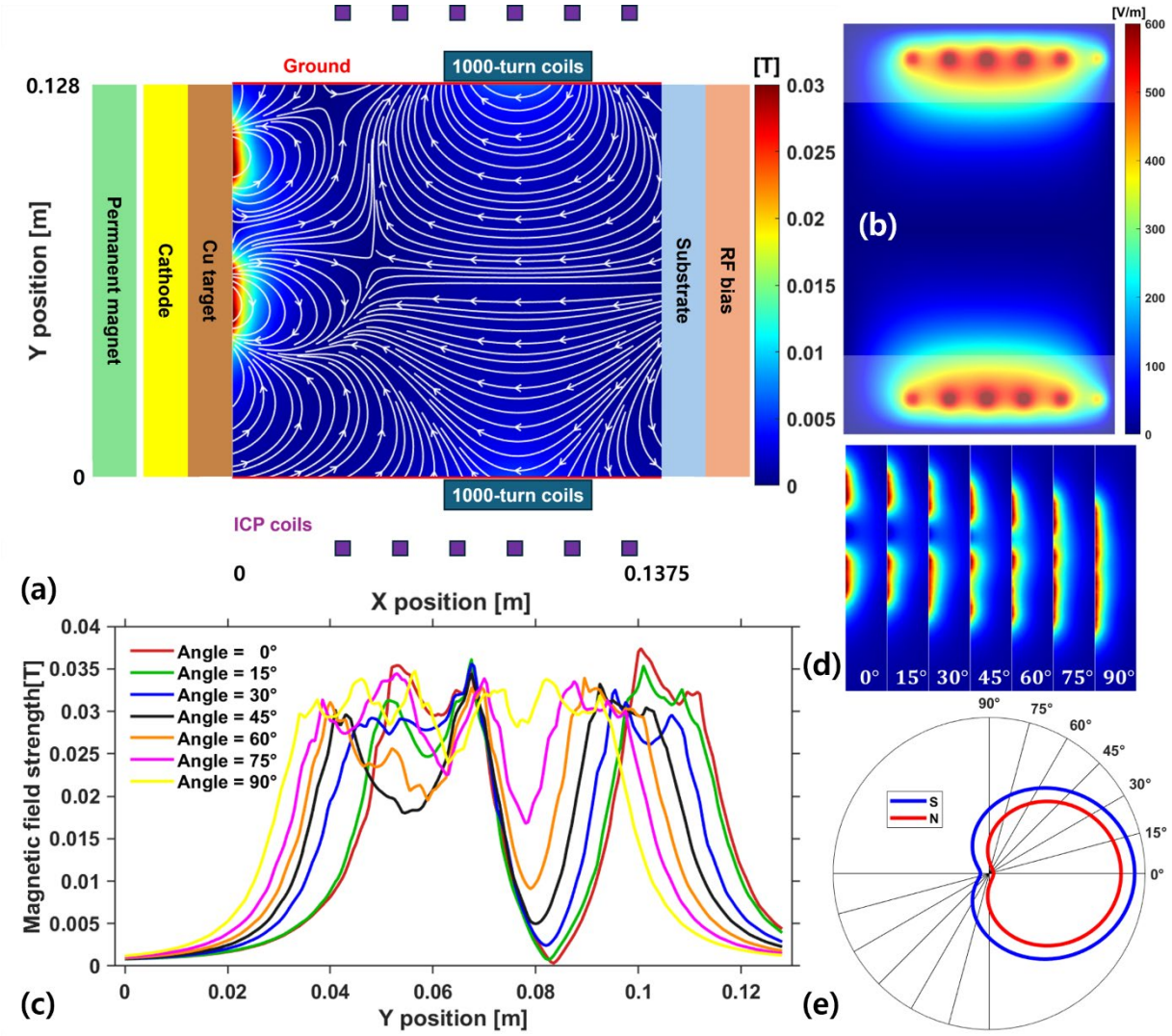

Figure 6. (a) Schematic diagram of the IMPVD device, (b) calculation domain of the ICP coils, (c) magnetic field distribution at the target surface for different rotation angles, (d) Magnetic field distribution near the target for different rotation angles, and (e) symmetry in the cardioid shape magnet configuration.

The schematic diagram of the IMPVD device, where metal particles sputtered from the target are ionized in the high-density plasma and incident perpendicularly onto the wafer by the electric field, achieving higher anisotropy compared to other methods, is shown in Fig. 6a. The magnetic field generated by the cardioid-shaped permanent magnet is calculated using CST. Additionally, a DC bias

Preprints.org (www.preprints.org) | NOT PEER-REVIEWED | Posted: 9 December 2024 doi:10.20944/preprints202412.0631.v1

is applied to collide ion particles from the plasma with the target in order to sputter target particles. An RF ICP is used to generate high-density plasma, and the 6-turn coil is placed to ionize the sputtered metal particles. RF bias is applied to incident ionized target particles perpendicularly onto the wafer. The EM coils near the wafer, which induce the magnetic field to control the position of the incoming metal ions, are calculated using FEMM.

The simulation domain size is $0.1375\ \mathrm{m} \times 0.1280\ \mathrm{m}$, with grid spacing of $0.005\ \mathrm{m} \times 0.005\ \mathrm{m}$ and a time step of 1×10^{-11} s. Argon gas at one mTorr is used. The ICP is operated at a frequency of 10 MHz with 100 W power, a DC bias of -200 V or -400 V is applied, and an RF bias of 2.5 MHz with 10 V is applied. A current of 3 A is passed through the EM coil. Additionally, the side wall is grounded.

Figure 6b shows the electric field in the z-direction generated by the ICP coils. The translucent area represents the region where the electromagnetic field is calculated by considering additional cells outside the PIC simulation domain, while the opaque region is the area where particles are handled. Figure 6c shows the magnetic field strength on the target surface, extracted from CST calculations at 15° intervals from 0° to 90°. The magnetic field distribution around the target at each angle is shown in Fig. 6d. The reason for considering angles from 0° to 90° is that, as shown in Fig. 6e, the results between 90° and 180° can be calculated using symmetry.

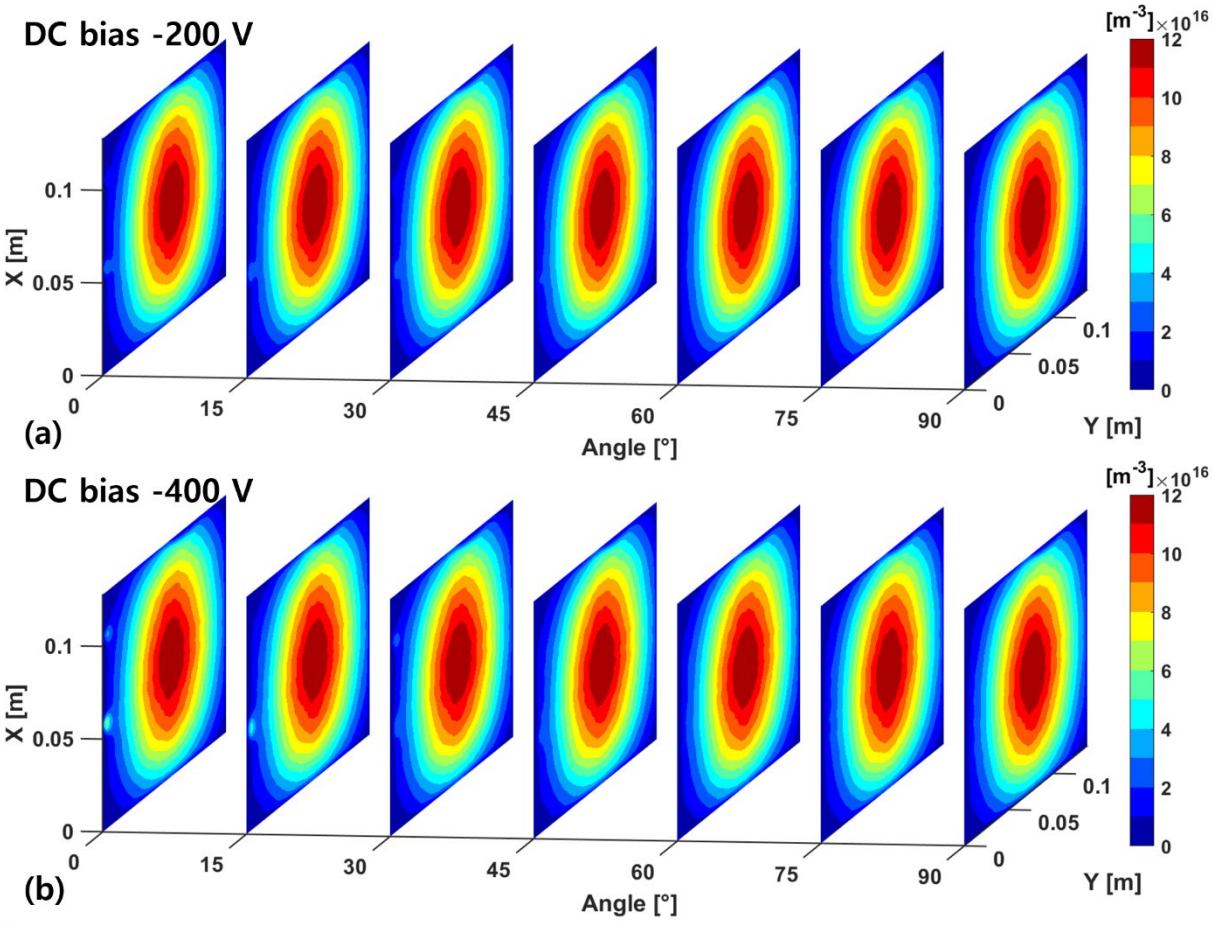

Figure 7. (a) Argon ion density profiles with a DC bias of -200 V and (b) with a DC bias of -400 V to the different magnetic field angles.

As shown in Fig. 7, the dense plasmas are generated primarily at the center by the ICP source, and the plasma densities slightly increase around the magnets. At -400 V, the plasma densities around the magnets are slightly higher than -200 V. As shown in Figs. 6c and 6d, the magnetic field distribution becomes relatively uniform around 60°, and plasmas at this angle do not experience an increase in density around the magnets.

Preprints.org (www.preprints.org) | NOT PEER-REVIEWED | Posted: 9 December 2024 doi:10.20944/preprints202412.0631.v1

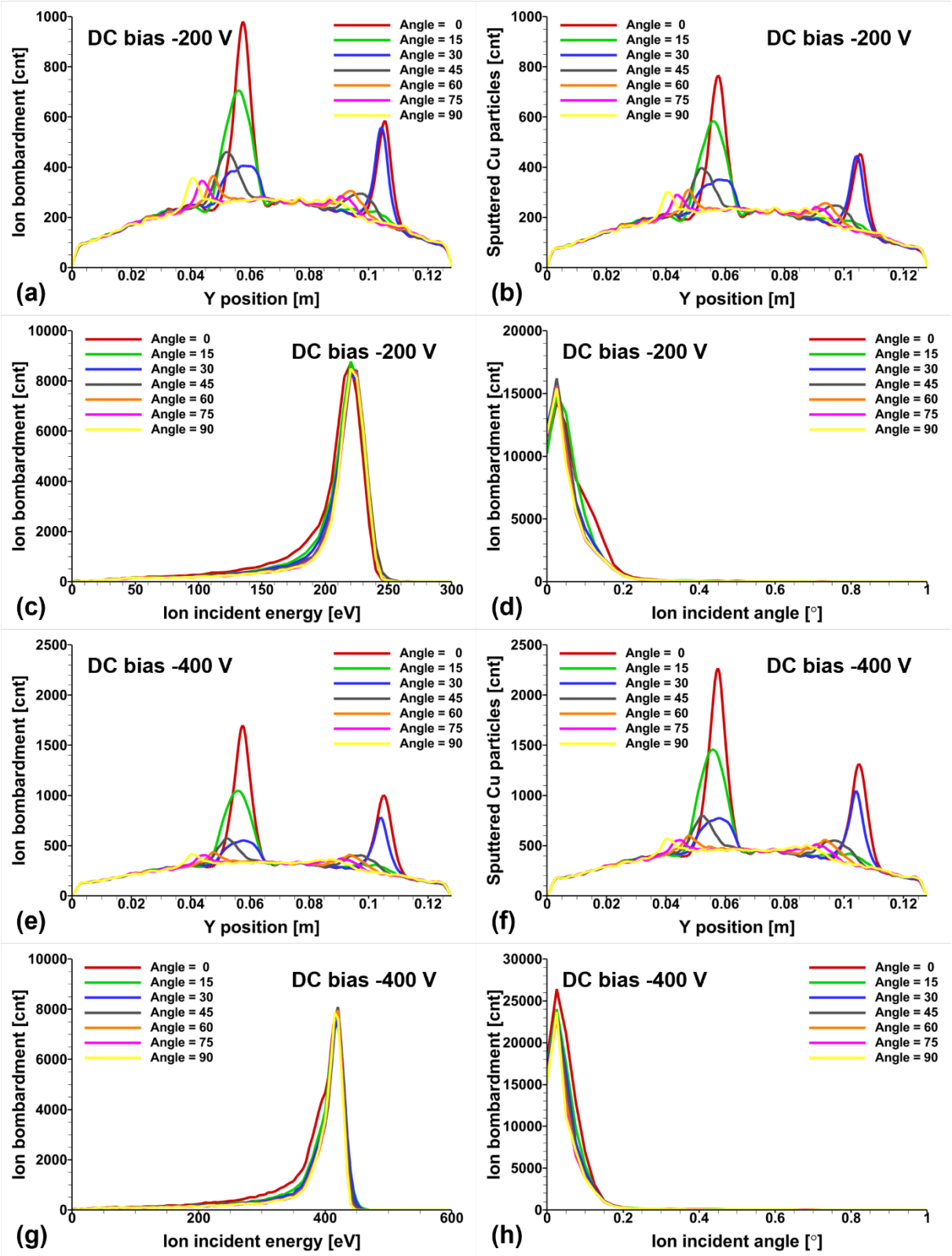

Figure 8. For DC biases of -200 V and -400 V, ion bombardment distributions with respect to space, sputtered particle distributions with respect to space, ion bombardment distributions with respect to the ion incident energy, and ion bombardment distributions with respect to the ion incident angle.

Although there seems to be no significant difference between -200 V and -400 V DC bias voltages when only considering plasma density, as shown in Fig. 8, there is a notable difference in the ion incident energy distribution. The ion acceleration due to the difference between the -200 V and -400 V DC bias voltages and the plasma potential results in an incident ion energy distribution that is

Preprints.org (www.preprints.org) | NOT PEER-REVIEWED | Posted: 9 December 2024 doi:10.20944/preprints202412.0631.v1

slightly higher than each bias voltage. As shown in the Yamamura formula in Fig. 5b, for sputtering yield to exceed 1, the argon ion must have an energy greater than 246 eV when incident on the copper target, which leads to a significant difference in sputtering yield. As seen in Fig. 8c, in the -200 V DC bias case, there is not much ion bombardment above 246 eV, resulting in smaller sputtered Cu particles in Fig. 8b compared to ion bombardment in Fig. 8a. In contrast, in the -400 V DC bias case shown in Fig. 8g, there is a higher amount of ion bombardment above 246 eV, leading to larger sputtered Cu particles in Fig. 8f compared to ion bombardment in Fig. 8e.

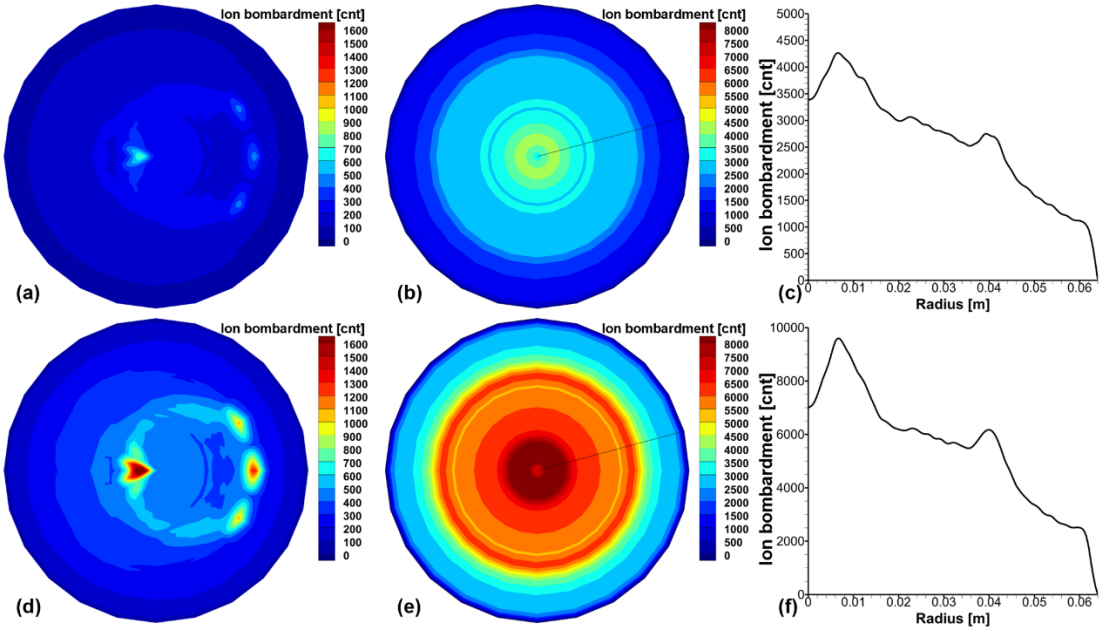

Figure 9. At -200 V DC bias, (a) ion bombardment on target with a stationary magnet, (b) ion bombardment on target with a rotating magnet, and (c) ion bombardment as a function of radial position. At -400 V DC bias, (d) ion bombardment on target with a stationary magnet, (e) ion bombardment on target with a rotating magnet, and (f) ion bombardment as a function of radial position.

Using the IEAD obtained from Fig. 8, the distribution of the ion bombardment for each angle of the magnet is transformed into a polar coordinate system, as shown in Fig. 9. Rotating Fig. 9a results in Fig. 9b, and the data extracted along the black solid line is shown in Fig. 9c. This calculation is performed because the values of the electric and magnetic fields vary with the rotation angle of the magnet, so the distribution of sputtered particles is calculated separately for each angle. Since the target rotates, this distribution is rotated to make it symmetric. Plasma density and electric and magnetic field data are used as fixed values in the DSMC simulation. This approach helps avoid heavy computations in the 3D field and allows the sputtered particle calculation to be performed in 3D.

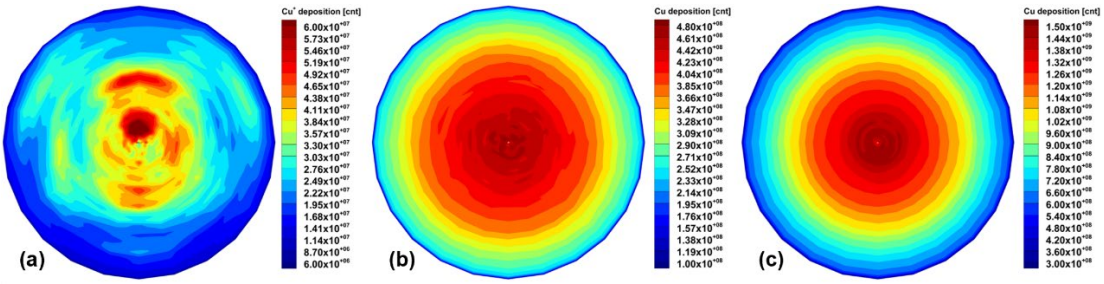

Figure 10. When the DC bias is -200 V, (a) Cu ions deposited on the substrate, (b) Cu atoms deposited on the substrate, and (c) Cu atoms deposited on the substrate without considering collisions.

Preprints.org (www.preprints.org) | NOT PEER-REVIEWED | Posted: 9 December 2024 doi:10.20944/preprints202412.0631.v1

When comparing Fig. 10b and 10c, it is observed that the number of Cu particles reaching the wafer is relatively smaller when collisions are taken into account. The case considering collisions shows better uniformity compared to the case without collisions. Since Cu particles are neutral, they are unaffected by the EM coil and directly reach the wafer. In the case of Cu ions in Fig. 10a, the amount reaching the wafer is about eight times smaller than the Cu particles. This is because the Cu ions are not sufficiently ionized, as the Ar ion density is relatively low at $1 \times 10^{17}\ \mathrm{m}^{-3}$. Due to computational limitations, the ICP power was reduced in the simulation, resulting in a low Ar ion density and consequently fewer Cu ions being produced. To better understand the collision rates and the density distribution of each species, it will be necessary to adjust the simulation conditions to increase plasma generation and observe the results.

To simplify the problem, a DC bias of -210 V is applied, and the RF bias is combined with a DC voltage of -20 V and 50 V at a frequency of 2.5 MHz. The distribution of the permanent magnet is set to the same as shown in Fig. 6, but the magnetic field strength is doubled. Under these conditions, EM coils and ICP coils are not used. PIC simulations are first performed, and the resulting potential, as well as the distributions of electrons and argon ions, are shown in Fig. 11.

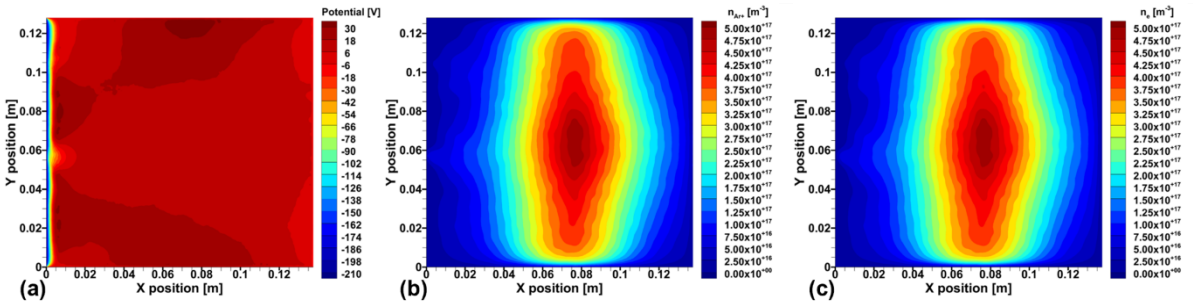

Figure 11. (a) Potential profile, (b) argon ion density distribution, and (c) electron density distribution.

Using these results, simulations are performed by changing the rate coefficient for the charge exchange between Ar ions and Cu atoms, as listed in Table 1. Three cases with rate coefficients of $1 \times 10^{-15}\ \mathrm{m}^3/\mathrm{s}$, $1 \times 10^{-14}\ \mathrm{m}^3/\mathrm{s}$, and $5 \times 10^{-14}\ \mathrm{m}^3/\mathrm{s}$ are considered, and the results of the DSMC simulations are shown in Fig. 12. The higher the rate coefficient for charge exchange, the fewer Cu atoms there are, and the more Cu ions are present. Additionally, when the charge exchange has a higher collision rate, the number of Cu atoms decreases, which is turn reduced the collision rate for ionization.

Preprints.org (www.preprints.org) | NOT PEER-REVIEWED | Posted: 9 December 2024 doi:10.20944/preprints202412.0631.v1

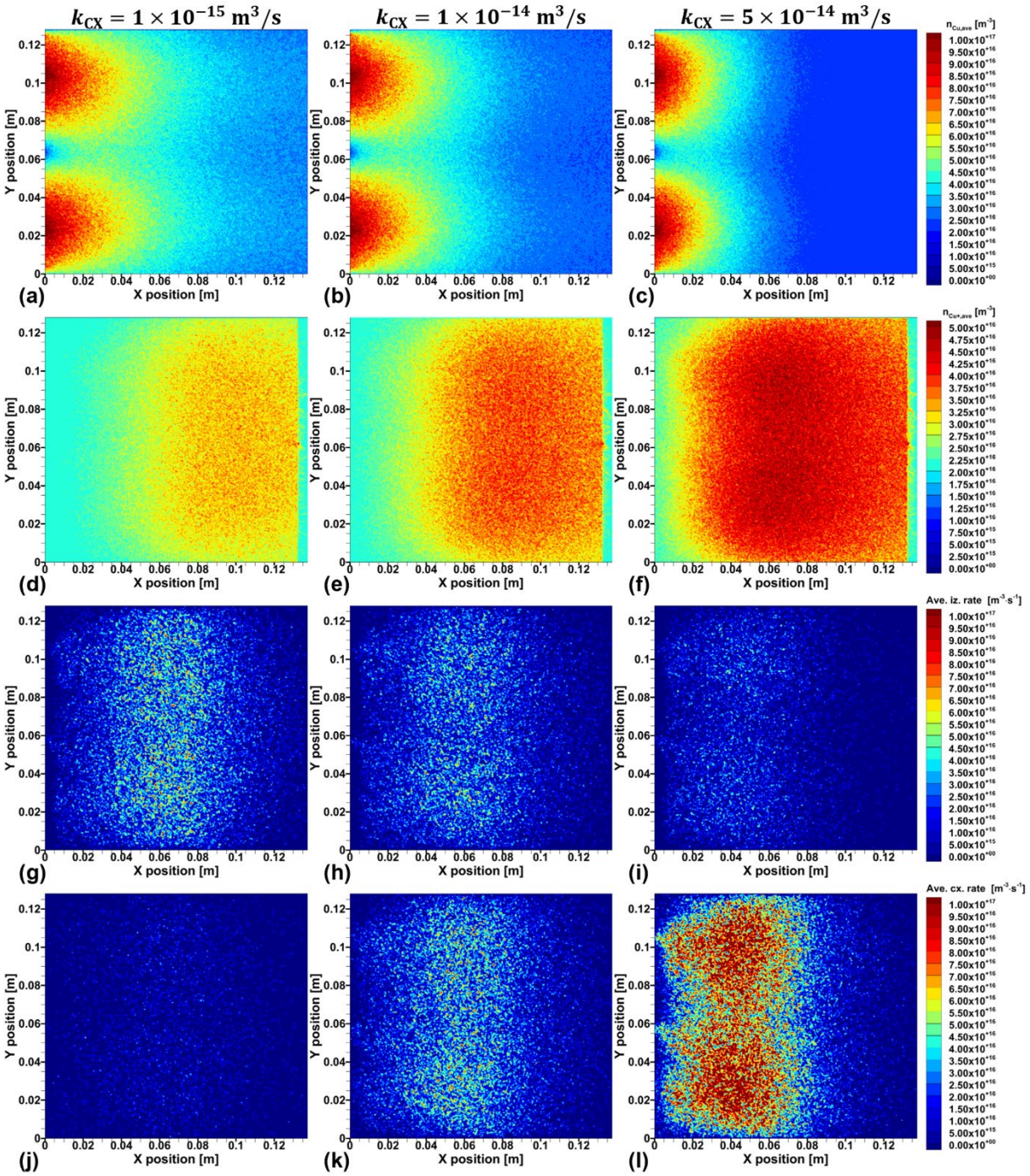

Figure 12. For the different rate coefficients of the charge exchange, 25-period averaged distributions of (a-c) Cu atom density, (d-f) Cu ion density, (g-i) ionization rate and (j-l) charge exchange rate.

From this result, it is clear that obtaining accurate cross-section data for the charge exchange reaction is important. Another point to consider is that the simulation of sputtered particles assumes the immobile plasma in the background, meaning that the potential distribution is almost fixed, and as a result, the motion of the generated Cu ions is not accurately represented. Therefore, further research considering the coupling between the plasma and sputtered particles is necessary.

5. Conclusions

This study simulated the RF magnetron sputtering process with a rotating target in an IMPVD system by coupling PIC and DSMC methods. The multi-step simulation methodology was introduced, and the results from a complex system consisting of DC bias, RF bias, ICP coils,

Preprints.org (www.preprints.org) | NOT PEER-REVIEWED | Posted: 9 December 2024 doi:10.20944/preprints202412.0631.v1

permanent magnet, and EM coils were analyzed to determine the ion bombardment and sputtered metal yield, as well as the deposition profiles of ions and neutral species. Furthermore, sputtering yield under different DC bias conditions was explained using the Yamamura formula, and tests were performed by varying the charge exchange rate coefficient to examine the spatial distribution of Cu and Cu ions, as well as the ionization rate and charge exchange rate contributions.

Author Contributions: The following statements should be used "Conceptualization, H.J.L. and H.J.K.; methodology, M.Y.H.; software, M.Y.H.; validation, H.J.L.,M.Y.H. and H.J.K.; formal analysis, H.J.L. and C.C.; investigation, C.C. and M.Y.H.; resources, H.J.L.; data curation, C.C. and M.Y.H.; writing—original draft preparation, C.C.; writing—review and editing, H.J.L.; visualization, C.C. and M.Y.H.; supervision, H.J.L.; project administration, H.J.L. and H.J.K.; funding acquisition, H.J.L. and H.J.K. All authors have read and agreed to the published version of the manuscript.

Funding: This research was supported by Samsung Electronics in 2016.

Institutional Review Board Statement: Not applicable.

Informed Consent Statement: Not applicable.

Data Availability Statement: data is unavailable and confidential.

Conflicts of Interest: The authors declare no conflicts of interest. The funders had no role in the design of the study; in the collection, analyses, or interpretation of data; in the writing of the manuscript; or in the decision to publish the results.

References

1. Gudmundsson, J. T. Physics and technology of magnetron sputtering discharge. *Plasma sources Sci. Technol.* **2020**, *29*, 113001.
2. Anders, A. Tutorial: Reactive high power impulse magnetron sputtering (R-HiPIMS). *J. Appl. Phys.* **2017**, *121*, 171101.
3. Liu, S.; Li, X.; Hao, Y.; Li, X.; Liu, F. Effect of magnetron sputtering process parameters on the conductivity of thin metal film. *AIP Advances* **2023**, *13*, 095326.
4. Wang, M.-C.; Chen, C.-Y.; Hsi, C.-S.; Wu, N.-C. Influence of deposition parameters on the dielectric properties of rf magnetron sputtered $Ba(Zr_xTi_{1-x})O_3$ thin films. *J. Eur. Ceram. Soc.* **2003**, *23*, 2307-2314.
5. Torii, K.; Kaga, T.; Takeda, E. Dielectric Properties of RF-Magnetron-Sputtered $(Ba,Pb)(Zr,Ti)O_3$ Thin Films. *Jpn. J. Appl. Phys.* **1992**, *31*, 2989-2991.
6. Prabakar, K.; Park, A.; Cho, N.; Lee, W. I.; Hwangbo, C. K.; Lee, J. G.; Lee, C. rf-Magnetron sputter deposited ZrO_2 dielectrics for metal-insulator-semiconductor capacitors. *Vacuum* **2008**, *82*, 1367-1370.
7. Zhao, H.; Xie, J.; Mao, A. Effects of Bottom Layer Sputtering Pressures and Annealing Temperatures on the Microstructures, Electrical and Optical Properties of Mo Bilayer Films Deposited by RF/DC Magnetron Sputtering. *Appl. Sci.* **2019**, *9*, 1395.
8. Helmersson, U.; Lattemann, M.; Bohlmark, J.; Ehiasarian, A. P.; Gudmundsson, J. T. Ionized Physical Vapor Deposition (IPVD): A Review of Technology and Applications. *Thin Solid Films* **2006**, *513*, 1-24.
9. Lu, J.; Kushner, M. J. Trench filling by ionized metal physical vapor deposition. *J. Vac. Sci. Technol. A* **2001**, *19*, 2652-2663.
10. Iseki, T. Flat erosion magnetron sputtering with a moving unbalanced magnet. *Vacuum* **2006**, *80*, 662-666.
11. Fu, C.; Yang, C.; Han, L.; Chen, H. The thickness uniformity of films deposited by magnetron sputtering with rotation and revolution. *Surf. Coat. Technol.* **2006**, *200*, 3687-3689.
12. Demaray, R. E.; Helmer, J. C.; Anderson, R. L.; Park, Y. H.; Cochran, R. R.; Hoffman, V. E. Rotating sputtering apparatus for selected erosion. United States Patent, US5252194A, **1993**.
13. Hur, M. Y.; Oh, S.; Kim, H. J.; Lee, H. J. Numerical Analysis of the Incident Ion Energy and Angle Distribution in the DC Magnetron Sputtering for the Variation of Gas Pressure, *Appl. Sci. Converg. Technol.* **2018**, *27*, 19-22.
14. Hur, M. Y.; Kim, J. S.; Lee, H. J. The effect of negative ions from the target on thin film deposition in a direct current magnetron sputtering system. *Thin Solid Films* **2015**, *587*, 3-7.
15. Jo, Y. H.; Park, H. S.; Hur, M. Y.; Lee, H. J. Curved-boundary particle-in-cell simulation for the investigation of the target erosion effect of DC magnetron sputtering system. *AIP Advances* **2020**, *10*, 125224.
16. Jo, Y. H.; Cheon, C.; Park, H.; Hur, M. Y.; Lee, H. J. Multi-dimensional electrostatic plasma simulations using the particle-in-cell method for the low-temperature plasmas for materials processing. *J. Korean Phys. Soc.* **2022**, *80*, 787-798.

Preprints.org (www.preprints.org) | NOT PEER-REVIEWED | Posted: 9 December 2024 doi:10.20944/preprints202412.0631.v1

17. Jo, Y. H.; Cheon, C.; Park, H.; Lee, H. J. Particle-in-Cell Simulations for the Improvement of the Target Erosion Uniformity by the Permanent Magnet Configuration of DC Magnetron Sputtering Systems. *Coatings* **2023**, *13*, 749.
18. Meeker, D. C. Finite Element Method Magnetics, Version 4.2 (28Feb2018 Build), https://www.femm.info.
19. CST Studio Suite 2014, CST AG, 2014.
20. Hur, M. Y.; Parallelization of Particle-in-Cell Simulation and Its Applications to Low Temperature Processing Plasmas and Nanopowder Synthesis. PhD Dissertation, Pusan National University, Busan, 2018.
21. Jo, Y. H.; 3D Particle-In-Cell Simulation of the Plasma Kinetics and Instabilities in Cross-Field Discharges. PhD Dissertation, Pusan National University, Busan, 2020.
22. Cheon, C.; Plasma Instabilities and Coherent Turbulent Structures in the Cross-Field Plasma Devices. PhD Dissertation, Pusan National University, Busan, 2024.
23. Baxter, J. P.; Schick, G. A.; Singh, J.; Kobrin, P. H.; Winograd, N. Angular distributions of sputtered particles. *J. Vac. Sci. Technol. A* **1986**, *4*, 1218-1221.
24. Yamamura, Y.; Tawara, H. Energy dependence of ion-induced sputtering yields from monatomic solids at normal incidence. *At. Data Nucl. Data Tables* **1996**, *62*, 149-253.
25. Eckstein, W.; Preuss, R. New fit formulae for the sputtering yield. *J. Nucl. Mater.* **2003**, *320*, 209-213.
26. Behrisch, R.; Eckstein, W. Sputtering by Particle Bombardment, Experiments and Computer Calculations from Threshold to MeV Energies, 1st ed.; Springer: Garching, Germany, 2007.
27. SIGLO database, www.lxcat.net, retrieved on November 20, 2024.
28. Grapperhaus, M. J.; Krivokapic, Z.; Kushner, M. J. Design issues in ionized metal physical vapor deposition of copper. *J. Appl. Phys.* **1998**, *83*, 35-43.

Disclaimer/Publisher's Note: The statements, opinions and data contained in all publications are solely those of the individual author(s) and contributor(s) and not of MDPI and/or the editor(s). MDPI and/or the editor(s) disclaim responsibility for any injury to people or property resulting from any ideas, methods, instructions or products referred to in the content.